Bimodal or quadrimodal? Statistical tests for the shape of fault patterns

David Healy[1*] & Peter Jupp[2]

[1]School of Geosciences, King's College, University of Aberdeen, Aberdeen AB24 3UE Scotland

[2]School of Mathematics & Statistics, University of St Andrews, St Andrews KY16 9SS Scotland

[*]Corresponding author e-mail: d.healy@abdn.ac.uk

Abstract

Natural fault patterns, formed in response to a single tectonic event, often display significant variation in their orientation distribution. The cause of this variation is the subject of some debate: it could be 'noise' on underlying conjugate (or bimodal) fault patterns or it could be intrinsic 'signal' from an underlying polymodal (e.g. quadrimodal) pattern. In this contribution, we present new statistical tests to assess the probability of a fault pattern having two (bimodal, or conjugate) or four (quadrimodal) underlying modes. We use the eigenvalues of the 2nd and 4th rank orientation tensors, derived from the direction cosines of the poles to the fault planes, as the basis for our tests. Using a combination of the existing fabric eigenvalue (or modified Flinn) plot and our new tests, we can discriminate reliably between bimodal (conjugate) and quadrimodal fault patterns. We validate our tests using synthetic fault orientation datasets constructed from multimodal Watson distributions, and then assess six natural fault datasets from outcrops and earthquake focal plane solutions. We show that five out of six of these natural datasets are probably quadrimodal. The tests have been implemented in the R language and a link is given to the authors' source code.

1. Introduction

1.1 Background

Faults are common structures in the Earth's crust, and they rarely occur in isolation. Patterns of faults, and other fractures such as joints and veins, control the bulk transport and mechanical properties of the crust. For example, arrays of low permeability (or 'sealing') faults in a rock matrix of higher permeability can produce anisotropy of permeability and preferred directions of fluid flow. Arrays of weak faults can similarly produce anisotropy – i.e. directional variations – of bulk strength. It is important to understand fault patterns, and quantifying the geometrical attributes of any pattern is an important first step. Faults, taken as a class of brittle shear fractures, are often assumed to form in conjugate arrays, with fault planes more or less evenly distributed about the largest principal compressive stress, σ_1, and making an acute angle with it. This model, an amalgam of theory and empirical observation, predicts that conjugate fault planes intersect along the line of σ_2 (the intermediate principal stress) and the fault pattern overall displays bimodal symmetry (Figure 1a). A fundamental limitation of this model is that these fault patterns can only ever produce a plane strain (intermediate principal strain $\varepsilon_2 = 0$), with no extension or shortening in the direction of σ_2. This kinematic limitation is inconsistent

with field and laboratory observations that document the existence of polymodal or quadrimodal fault patterns, and which produce triaxial strains in response to triaxial stresses (e.g. Aydin & Reches, 1982; Reches, 1978; Blenkinsop, 2008; Healy et al., 2015; McCormack & McClay, 2018). Polymodal and quadrimodal fault patterns possess orthorhombic symmetry (Figure 1b & 1c).

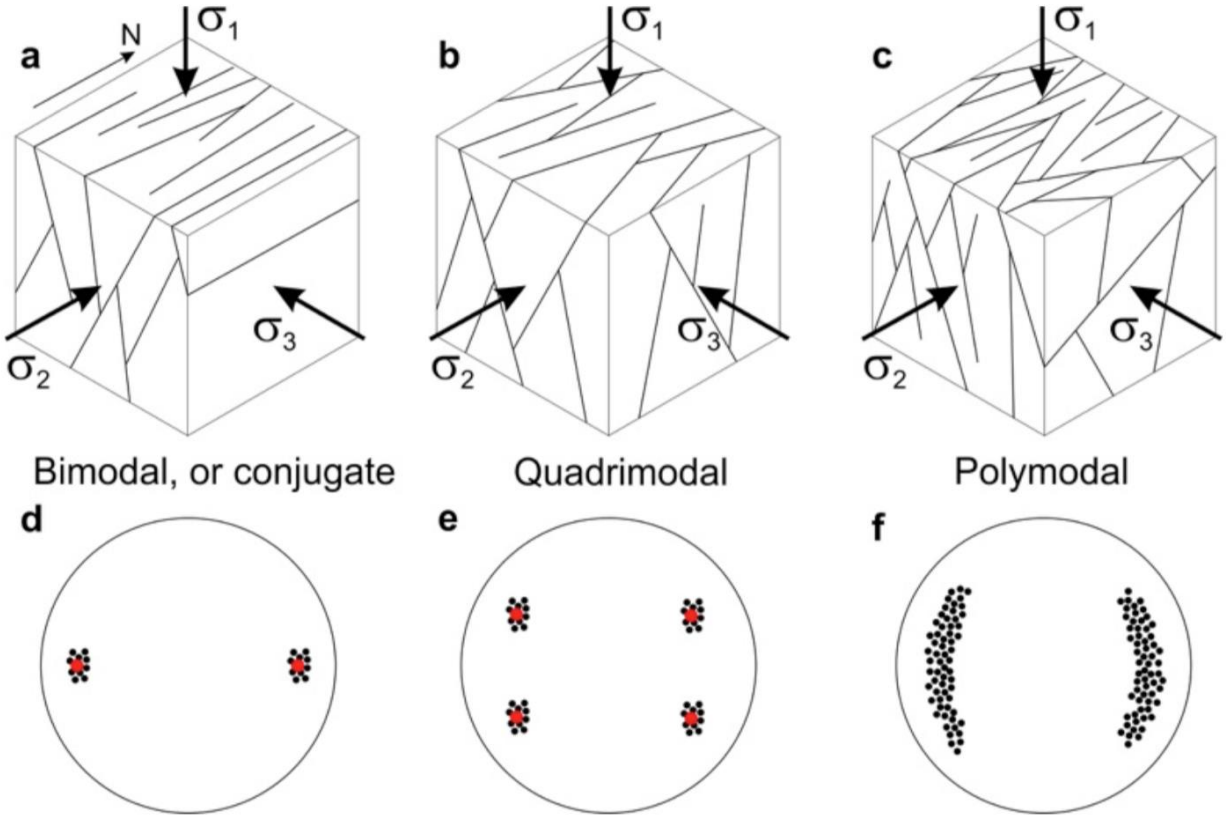

Figure 1. Schematic diagrams to compare conjugate fault patterns displaying bimodal symmetry with quadrimodal and polymodal fault patterns displaying orthorhombic symmetry. **a-c**) Block diagrams showing patterns of normal faults and their relationship to the principal stresses. **d-f**) Stereographic projections (equal area, lower hemisphere) showing poles to fault planes for the models shown in a-c. Natural examples of all three patterns have been found in naturally deformed rocks.

Fault patterns are most often visualised through maps of their traces and equal-angle (stereographic) or equal-area projections of poles to fault planes or great circles. Azimuthal projection methods (hereafter 'stereograms') provide a measure of the orientation distribution, including the attitude and the shape of the overall pattern. However, these plots can be unsatisfactory when they contain many data points, or the data are quite widely dispersed. Woodcock (1977) developed the idea of the fabric shape, based on the fabric or orientation tensor of Scheidegger (1965). The eigenvalues of this 2nd rank tensor can be used in a modified Flinn plot (Flinn, 1962; Ramsay, 1967) to discriminate between clusters and girdles of poles. These plots can be useful for three of the five possible fabric symmetry classes – spherical, axial and orthorhombic – because the three fabric eigenvectors coincide with the three symmetry axes. However, there are issues with the interpretation of distributions that are not uniaxial (Woodcock, 1977). We address these issues in this paper. Reches (Reches, 1978; Aydin &

Reches, 1982; Reches, 1983; Reches & Dieterich, 1983) has exploited the orthorhombic symmetry of measured quadrimodal fault patterns to explore the relationship between their geometric/ kinematic attributes and tectonic stress. More recently, Yielding (2016) measured the branch lines of intersecting normal faults from seismic reflection data and found they aligned with the bulk extension direction – a feature consistent with their formation as polymodal patterns. Bimodal (i.e. conjugate) fault arrays have branch lines aligned perpendicular to the bulk extension direction.

1.2 Rationale

The fundamental underlying differences in the symmetries of the two kinds of fault pattern – bimodal/bilateral and polymodal/orthorhombic – suggest that we should test for this symmetry using the orientation distributions of measured fault planes. The results of such tests may provide further insight into the kinematics and/or dynamics of the fault-forming process. This paper describes new tests for fault pattern orientation data, and includes the program code for each test written in the R language (R Core Team, 2017). The paper is organised as follows: the next section (2) reviews the kinematic and mechanical issues raised by conjugate and polymodal fault patterns, and in particular, the implications for their orientation distributions. Section 3 describes the datasets used in this study, including synthetic and natural fault orientation distributions. Section 4 presents tests for assessing whether an orientation distribution has orthorhombic symmetry, including a description of the mathematics and the R code. The examples used include synthetic orientation datasets of known attributes (with and without added 'noise') and natural datasets of fault patterns measured in a range of rock types. A Discussion of issues raised is provided in Section 5, and is followed by a short Summary. The R code is available from http://www.mcs.st-andrews.ac.uk/~pej/2mode_tests.html

2. Bimodal (conjugate) versus quadrimodal fault patterns

Conjugate fault patterns should display bimodal or bilateral symmetry in their orientation distributions on a stereogram, and ideally show evidence of central tendency about these two clusters (Figure 1d; Healy et al., 2015). Quadrimodal fault patterns should show orthorhombic symmetry and, ideally, evidence of central tendency about the four clusters of poles on stereograms (Figure 1e). More general polymodal patterns should show orthorhombic symmetry with an even distribution of poles in two arcs (Figure 1f). For data collected from natural fault planes some degree of intrinsic variation, or 'noise', is to be expected. Two natural example datasets are shown in Figure 2. The Gruinard dataset is from a small area (~ 5 m^2) in one outcrop of Triassic sandstone, and shows poles to deformation bands with small normal offsets (mm-cm). The Flamborough dataset is taken from Peacock & Sanderson (1992; their Figure 2a) and shows poles to normal faults in the Cretaceous chalk along a coastline section of about 1.8 km. The authors clearly state that the approximately E-W orientation of the coastline may have generated a sampling bias in the measured data (i.e. a relative under-representation of E-W oriented fault planes). Both datasets illustrate the nature of the problem addressed in this paper: given variable, incomplete and noisy data of different sample sizes, how can we assess the symmetry of the underlying fault pattern?

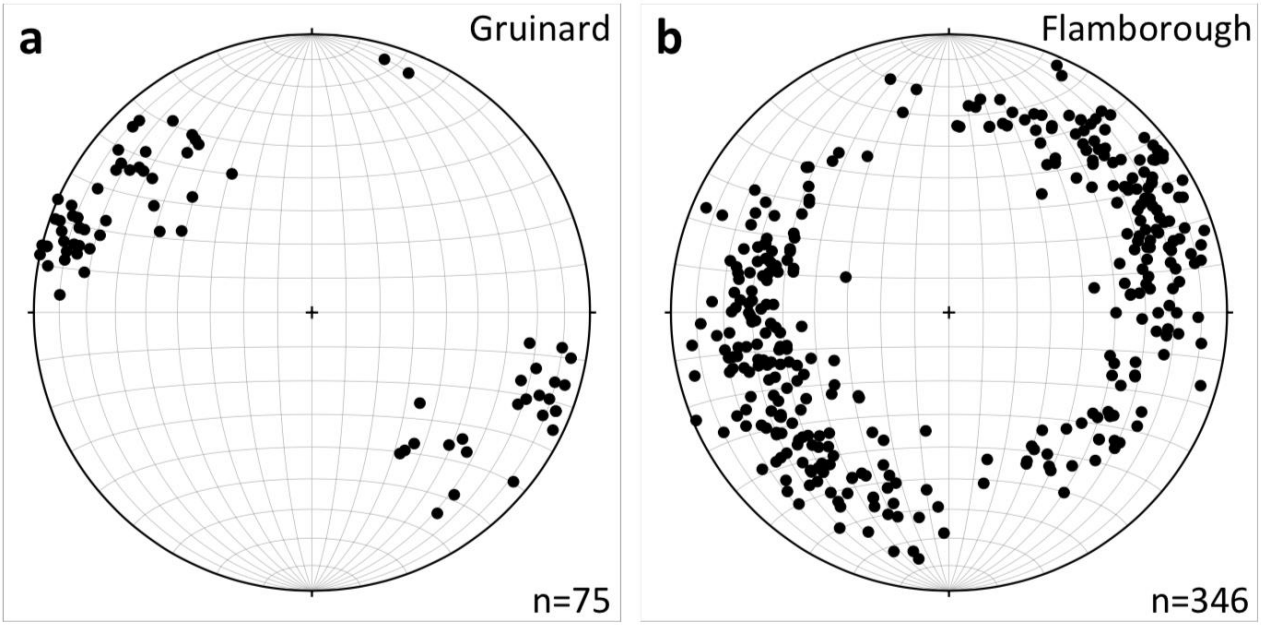

Figure 2. Stereographic projections (equal area, lower hemisphere) showing two natural fault datasets. a) Poles to deformation bands (small offset faults; *n*=75) measured in Triassic sandstones at Gruinard Bay, NW Scotland (Healy et al., 2006a, b). These data were collected from a small contiguous outcrop, approximately 10 m^2 in area. b) Poles to faults measured in Cretaceous chalk at Flamborough Head, NE England (*n*=346). These data have been taken from a figure published in Peacock & Sanderson (1992) and re-plotted in the same format as those from Gruinard.

3. Datasets used in this study

3.1. Synthetic datasets

We use two sets of synthetic data to test our new statistical methods, both based on the Watson orientation distribution (Fisher et al., 1987 section 4.4.4; Mardia & Jupp, 2000 section 9.4.2). This is the simplest non-uniform distribution for describing undirected lines, and has probability density

$$f(\pm\boldsymbol{x};\boldsymbol{\mu},\kappa) \propto exp\{\kappa(\boldsymbol{\mu}^{\boldsymbol{T}}\boldsymbol{x})^2\}$$

where κ is a measure of concentration (low κ = dispersed, high κ = concentrated) and $\boldsymbol{\mu}$ is the mean direction. To obtain a synthetic conjugate fault pattern dataset of size *n* we combined two datasets of size $n/2$, each from a Watson distribution, the two mean directions being separated by 60°. We generated synthetic bimodal datasets with κ = 10, 20, 50 and 100 and *n*=52 and 360 (Figure 3). This variation in κ provides a useful range of concentrations encompassing those observed in measured natural data, and can be considered as a measure of 'noise' within the distribution. Many natural datasets are often small due to limitations of outcrop size, and the two sizes of synthetic distribution (*n*=52 and 360) allow for this fact. For synthetic polymodal fault patterns, we generated quadrimodal datasets of size *n* by combining four Watson distributions of size $n/4$ with their mean directions separated by 60° in dip (as above) and 52°

130 in strike (see Healy et al., 2006a, b). By varying *n* from 52 to 360 we cater for comparisons with
131 smaller and larger natural datasets, and as for the synthetic bimodal datasets, we varied κ in
132 the range 10, 20, 50 and 100 (Figure 4).

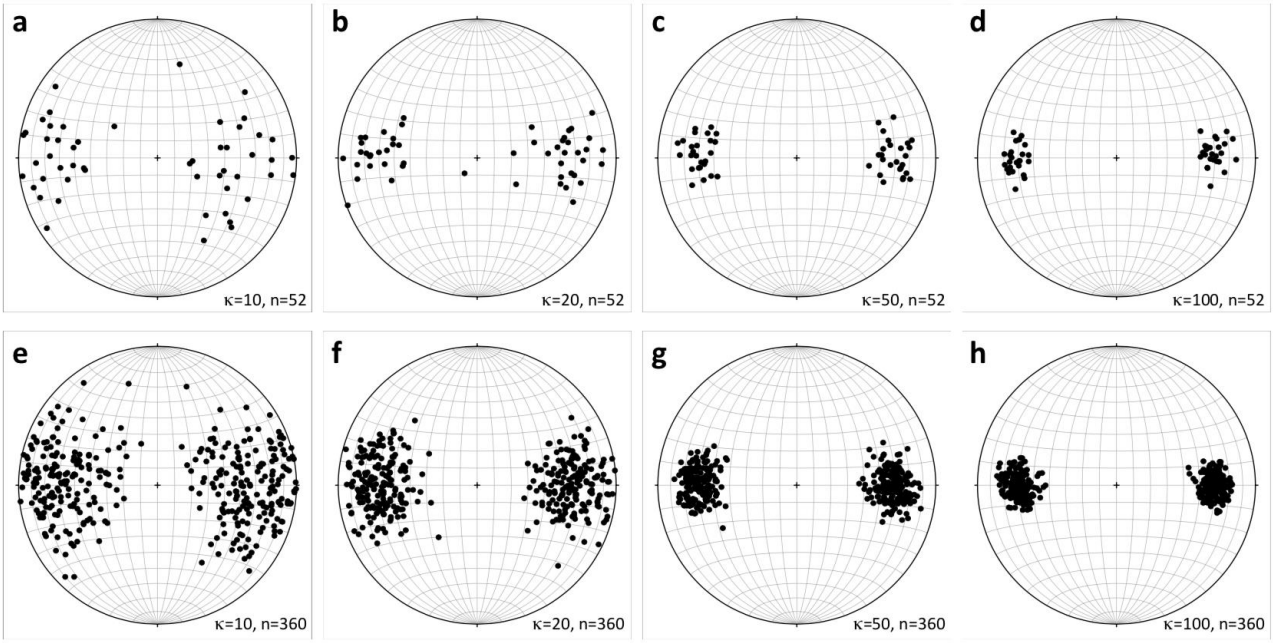

133

134 **Figure 3.** Stereographic projections (equal area, lower hemisphere) showing the eight
135 synthetic datasets designed to model conjugate (bimodal) fault patterns in this study. **a-d**)
136 Synthetic fault datasets derived from equal mixtures of two Watson distributions with mean
137 pole directions separated by an inter-fault dip angle of 60 degrees. These models represent a
138 'low fault count' scenario, with *n* = 52 and κ (the Watson dispersion parameter) varying from
139 10 to 100. **e-h**) These models represent a 'high fault count' scenario, with *n* = 360 and κ varying
140 from 10 to 100.

141

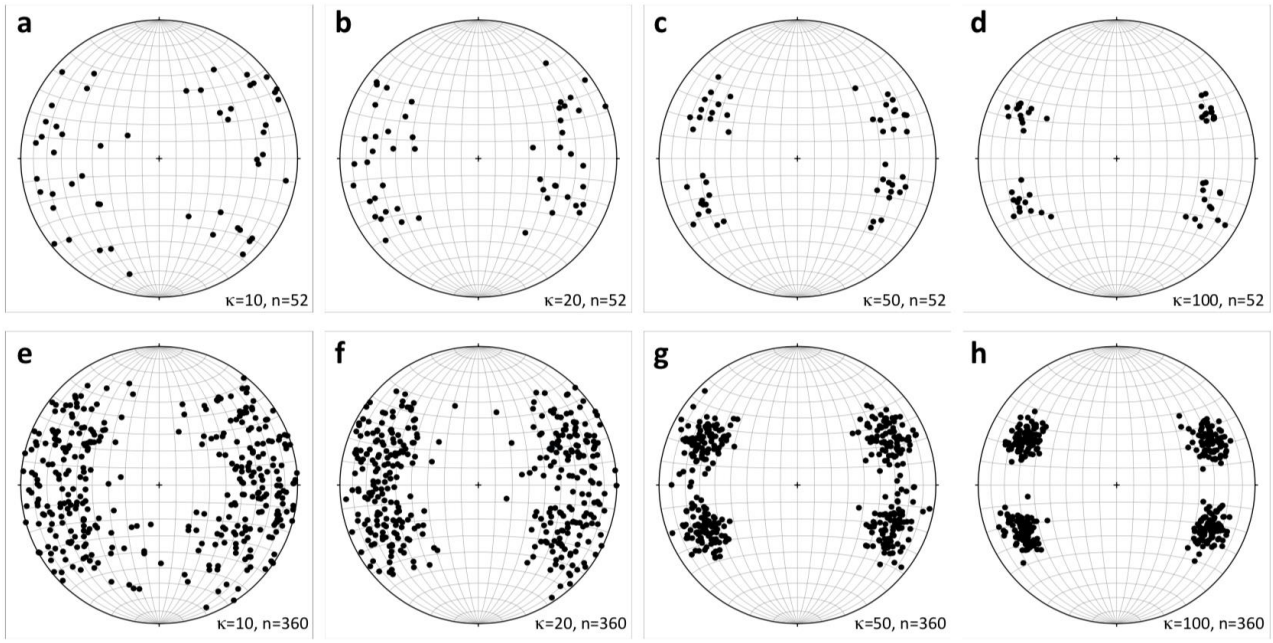

142

Figure 4. Stereographic projections (equal area, lower hemisphere) showing the eight synthetic datasets designed to model quadrimodal fault patterns in this study. **a-d**) Synthetic fault datasets derived from equal mixtures of four Watson distributions with mean pole directions separated by an inter-fault dip angle of 60 degrees and a strike separation of 52 degrees. These models represent a 'low fault count' scenario, with n = 52 and κ (the Watson dispersion parameter) varying from 10 to 100. **e-h**) These models represent a 'high fault count' scenario, with n = 360 and κ varying from 10 to 100.

3.2. Natural datasets

We use six natural datasets of fault plane orientations from regions that have undergone or are currently undergoing extension - i.e. we believe the majority of these faults display normal kinematics (Figure 5). The Gruinard dataset (Figure 5a) is from Gruinard Bay in NW Scotland (UK), and featured in previous publications (Healy et al., 2006a, b). The most important thing about this dataset is that the fault planes were all measured from a small area (~5 m^2) of contiguous outcrop of a single sandstone bed. This means it is highly unlikely that the orientation data are affected by any local stress variations and subsequent possible rotations. The data were measured in normal-offset deformation bands with displacements of a few millimetres to centimetres. The next three datasets have been digitised from published papers on normal faults in Utah (Figure 5b; Chimney Rock; Krantz, 1989), northern England (Figure 5c; Flamborough; Peacock & Sanderson, 1992) and Italy (Figure 5d; Central Italy; Roberts, 2007). In each case, the published stereograms were digitised to extract Cartesian (x,y) coordinates of the poles to faults, and these were then converted to plunge and plunge direction using the standard equations for the projection used (e.g. Lisle & Leyshon, 2004). Slight differences in the number of data plotted for each of these three with respect to the original publication arise due to the finite resolution of the digitised image of the stereograms. The last two datasets for the Aegean and Tibet (Figure 5e & f) are derived from earthquake focal mechanisms using the CMT catalogue (Ekström et al., 2012). In each case the steepest dipping nodal plane was selected in the absence of convincing evidence for low-angle normal faulting in these regions.

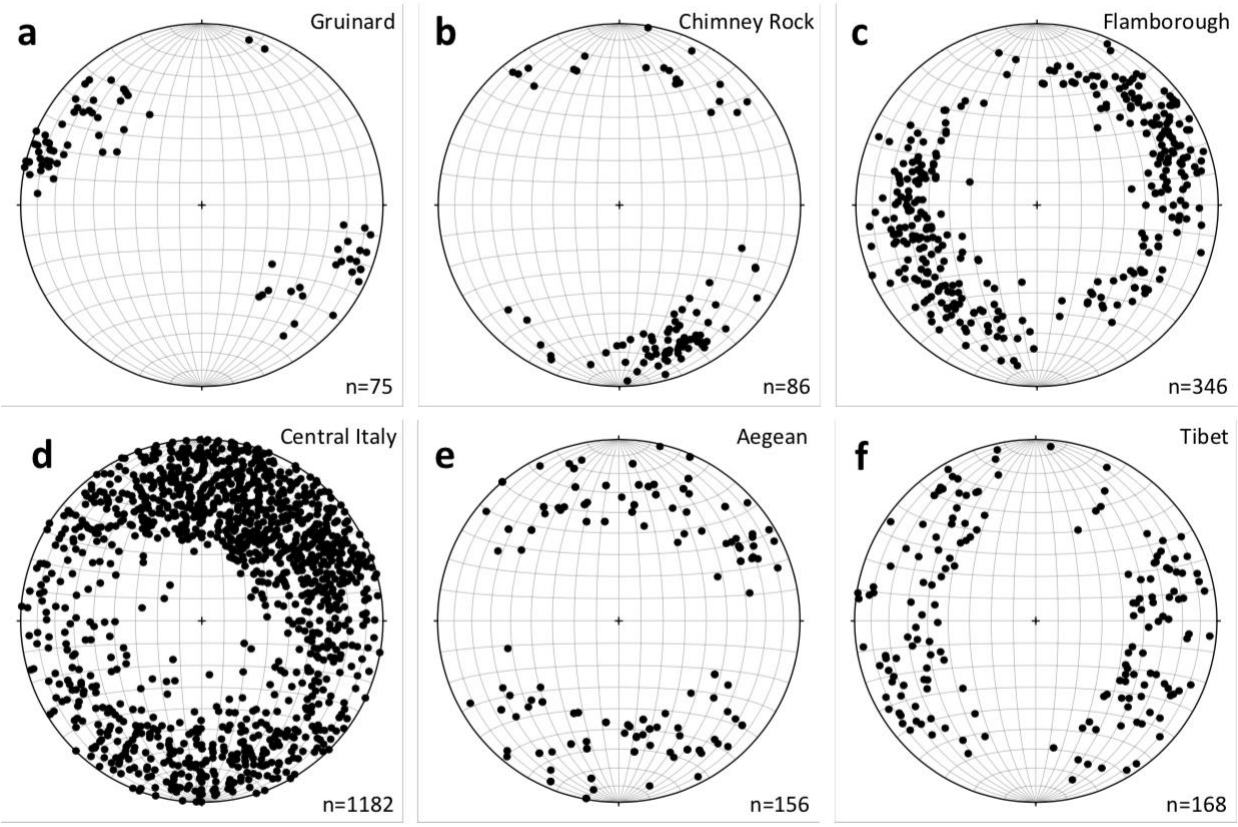

Figure 5. Stereographic projections (equal area, lower hemisphere) showing the six natural datasets used in this study. All plots show poles to faults, the majority of which are inferred to be normal. **a**) Data from deformation bands measured in faulted Triassic sandstones at Gruinard Bay, Scotland (Healy et al., 2006a; 2006b). **b**) Data from faults and measured in sandstones at Chimney Rock in the San Rafael Swell, Utah, USA. Data digitised from Krantz (1989). **c**) Data from faults measured in cliffs of Cretaceous chalk at Flamborough Head, NE England. Data digitised from Peacock & Sanderson (1992). **d**) Data from faults measured in the Apennines of Central Italy. Data digitised from Roberts (2007). **e**) Data from focal mechanism nodal planes derived from the CMT catalogue for the Aegean region (Ekström et al., 2012). **f**) Data from focal mechanism nodal planes derived from the CMT catalogue for the Tibet region (Ekström et al., 2012).

4. Testing for orthorhombicity

4.1 Eigenvalue fabric (modified Flinn) plots

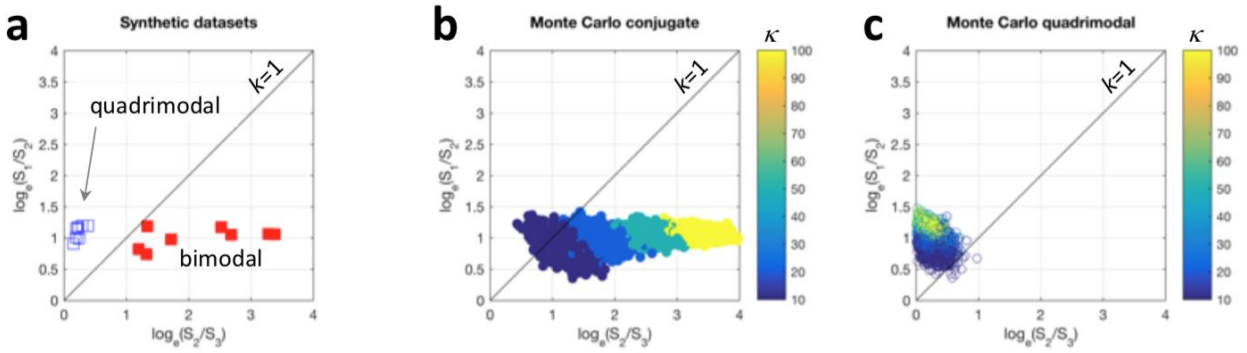

Figure 6. Graphs showing the ratios of eigenvalues of the orientation matrices for the synthetic datasets (Flinn, 1962; Ramsay, 1967; Woodcock, 1977). **a**) Synthetic conjugate (i.e. bimodal; filled red symbols) and quadrimodal (hollow blue symbols) fault data. Note that the conjugate and quadrimodal data lie either side of the line $k = 1$, where $k = \ln(S_1/S_2)/\ln(S_2/S_3)$. **b**) Eigenvalue ratios from a Monte Carlo simulation of conjugate fault orientations using the two Watson mixture model. 1000 simulations were run for each of four different κ values (10, 20, 50 and 100; a total of 4000 data points), corresponding to the range of the discrete datasets shown in a). **c**) Eigenvalue ratios from a Monte Carlo simulation of quadrimodal fault orientations using the four Watson mixture model. 1000 simulations were run for each of four different κ values (10, 20, 50 and 100; a total of 4000 data points), corresponding to the range of the discrete datasets shown in a).

We calculated the 2nd rank orientation tensor (Woodcock, 1977) for each of the synthetic datasets shown in Figures 3 and 4 (bimodal and quadrimodal, respectively). The eigenvalues of this tensor (S_1, S_2 and S_3, where S_1 is the largest and S_3 is the smallest) are used to plot the data on a modified Flinn diagram (Figure 6), with $\ln(S_2/S_3)$ on the x-axis and $\ln(S_1/S_2)$ on the y-axis. The points corresponding to the bimodal (shown in red) and quadrimodal (shown in blue) datasets lie in distinct areas. Bimodal (conjugate) fault patterns lie below the 1:1 line, on which $S_1/S_2 = S_2/S_3$. This is due to the S_3 eigenvalue being very low (near 0) for these distributions, which for high values of κ begin to resemble girdle fabric patterns confined to the plane of the eigenvectors corresponding to eigenvalues S_1 and S_2 (Woodcock, 1977). In contrast, the quadrimodal patterns lie above the 1:1 line, as S_3 for these distributions is large relative to the equivalent bimodal pattern (i.e. for the same values of κ and n). The modified Flinn plot therefore provides a potentially rapid and simple way to discriminate between bimodal (conjugate) and quadrimodal fault patterns. Note, however, that the spread of the bimodal patterns in Figure 6a along the x-axis is a function of the κ value of the underlying Watson distribution, with low values of κ – low concentration, highly dispersed – lying closer to the origin. Dispersed or noisy bimodal (conjugate) patterns may therefore lie closer to quadrimodal patterns (see Discussion below).

4.2 Randomisation tests using 2nd and 4th rank orientation tensors

4.2.1 Underlying distributions

To get a suitable general setting for our tests, we formalise the construction of the bimodal and quadrimodal datasets considered in Section 3.1. Whereas the datasets considered in Section 3.1

necessarily have equal numbers of points around each mode, for datasets arising from the distributions here, this is true only *on average*. The very restrictive condition of having a Watson distribution around each mode is relaxed here to that of having a circularly-symmetric distribution around each mode.

Suppose that axes $\pm\mathbf{x_1}, \ldots \pm\mathbf{x_n}$ are independent observations from some distribution of axes. If the parent distribution is thought to be multi-modal then two appealing models are:

(i) The **bimodal equal mixture model** can be thought of intuitively as obtained by 'pulling apart' a unimodal distribution into two equally strong modes angle α apart. More precisely, the probability density is:

$$f_2(\pm\mathbf{x};\ \{\pm\boldsymbol{\mu_1}, \pm\boldsymbol{\mu_2}\}) = \frac{1}{2}\{g(\pm\mathbf{x};\ \pm\boldsymbol{\mu_1}) + g(\pm\mathbf{x};\ \pm\boldsymbol{\mu_2})\}, \qquad (1)$$

where $\pm\boldsymbol{\mu}_1$ and $\pm\boldsymbol{\mu_2}$ are axes angle α apart, and $g(.;\ \pm\boldsymbol{\mu})$ is the probability density function of some axial distribution that has rotational symmetry about its mode $\pm\boldsymbol{\mu}$;

(ii) The **quadrimodal equal mixture model** can be thought of intuitively as obtained by 'pulling apart' a bimodal equal mixture distribution into two bimodal equal mixture distributions with planes angle γ apart, so that it has four equally strong modes. More precisely, the probability density is:

$$f_4(\pm\mathbf{x};\ \{\pm\boldsymbol{\mu_1}, \pm\boldsymbol{\mu_2}\}, \gamma) = \frac{1}{4}\sum_{\varepsilon,\eta} g\left(\pm\mathbf{x};\ \pm\boldsymbol{\mu}_{\varepsilon,\eta}\right), \qquad (2)$$

where

$$\boldsymbol{\mu}_{\epsilon,\eta} = \check{c}(c\boldsymbol{\nu_1} + \epsilon s\boldsymbol{\nu_2}) + \eta\check{s}\boldsymbol{\nu_3} \qquad (3)$$

with $c = \cos(\alpha/2), s = \sin(\alpha/2), \check{c} = \cos(\gamma/2), \check{s} = \sin(\gamma/2)$, $\cos(\alpha) = \boldsymbol{\mu}_1'\boldsymbol{\mu_2}$ and (ϵ, η) runs through $\{\pm 1\}^2$. If $\gamma = 0$, then (3) reduces to (2).

The problem of interest is to decide whether the parent distribution is (1) or (2).

4.2.2 The tests

Given axes $\pm\mathbf{x_1}, \ldots \pm\mathbf{x_n}$ we denote by $\pm\hat{\boldsymbol{\nu}}_1$ and $\pm\hat{\boldsymbol{\nu}}_3$, respectively, the largest and smallest principal axes of the orientation tensor. S_1 and S_3 are the eigenvalues of this matrix. We can also define

$$S_{11} = n^{-1}\sum_{i=1}^{n}(\hat{\boldsymbol{\nu}}_1'\mathbf{x}_i)^4, S_{33} = n^{-1}\sum_{i=1}^{n}(\hat{\boldsymbol{\nu}}_3'\mathbf{x}_i)^4.$$

S_1 and S_2 are the 2nd moments of $\pm\mathbf{x_1}, \ldots \pm\mathbf{x_n}$ along the 1st and 3rd principal axes, respectively, whereas S_{11} and S_{33} are the 4th moments along these principal axes. Therefore, both $S_1 - S_3$ and $S_{11} - S_{33}$ are measures of anisotropy of $\pm\mathbf{x_1}, \ldots \pm\mathbf{x_n}$.

Some algebra shows that

$$T_1 - T_3 = \cos(\gamma)\{E[x^2] - E[v^2]\}, \qquad (4)$$

where T_1 and T_3 are the population versions of S_1 and S_3, respectively, and $\pm x$ and $\pm v$ are the components of $\pm\mathbf{x}$ in the quadrimodal equal mixture model (2) along its 1st and 3rd principal axes, respectively. Then (4) gives

$$\cos(\gamma) \approx \frac{S_1 - S_3}{E[x^2] - E[v^2]}$$

and therefore, it is sensible to:

reject bimodality for *small* values of $S_1 - S_3$. (5)

Further algebra shows that

$$T_{11} - T_{33} = \cos(\gamma)\{E[x^4] - E[v^4]\}, \quad (6)$$

where T_{11} and T_{33} are the population versions of S_{11} and S_{33}, respectively. Then (6) gives

$$\cos(\gamma) \approx \frac{S_{11} - S_{33}}{E[x^4] - E[v^4]}$$

and so, it is sensible to:

reject bimodality for *small* values of $S_{11} - S_{33}$. (7)

The significance of tests (5) or (7) is assessed by comparing the observed value of the statistic with the randomisation distribution. This is achieved by creating a further B pseudo-samples (for a suitable positive integer B), in each of which the ith observation is obtained from $\pm x_i$ by rotating $\pm x_i$ about the closer of the 2 fitted modes through a uniformly distributed random angle. The p-value is taken as the proportion of the B+1 values of the statistic that are smaller than (or equal to) the observed value.

4.3 Results for synthetic datasets

Table 1 gives the p-values and corresponding decisions (at the 5% level) obtained by applying the tests to some synthetic datasets simulated from the bimodal equal mixture model. Table 2 does the same for some datasets simulated from the quadrimodal equal mixture model. In each case, both tests come to the correct conclusion.

True number of modes			**$S_1 - S_3$ test**		**$S_{11} - S_{33}$ test**	
	κ	n	p-value	# of modes	p-value	# of modes
2	10	52	0.37	2	0.51	2
2	10	360	0.27	2	0.33	2
2	20	52	0.66	2	0.69	2
2	20	360	0.20	2	0.25	2
2	50	52	0.45	2	0.48	2
2	50	360	0.35	2	0.42	2
2	100	52	0.34	2	0.41	2

2	100	360	0.60	2	0.63	2

Table 1. *p*-values and corresponding decisions at 5% significance level of randomisation tests of bimodality for bimodal equal mixtures of synthetic Watson distributions. *n*=total sample size. *B*=999 further randomisation samples per data set (see text for details).

True number of modes			**$S_1 - S_3$ test**		**$S_{11} - S_{33}$ test**	
	κ	n	*p*-value	# of modes	*p*-value	# of modes
4	10	52	0.00	> 2	0.00	> 2
4	10	360	0.00	> 2	0.00	> 2
4	20	52	0.00	> 2	0.00	> 2
4	20	360	0.00	> 2	0.00	> 2
4	50	52	0.00	> 2	0.00	> 2
4	50	360	0.00	> 2	0.00	> 2
4	100	52	0.00	> 2	0.00	> 2
4	100	360	0.00	> 2	0.00	> 2

Table 2. *p*-values and corresponding decisions at 5% significance level of randomisation tests of bimodality for quadrimodal equal mixtures of Watson distributions. *n*=total sample size. *B*=999 further randomisation samples per data set (see text for details).

4.4 Results for natural datasets

Table 3 gives the *p*-values and corresponding decisions (at the 5% level) obtained by applying the tests to the natural datasets discussed in Section 3.2. For each dataset, the two tests come to the same conclusion, which is plausible in view of Figure 5. Figure 7 shows the fabric eigenvalue plot for these datasets.

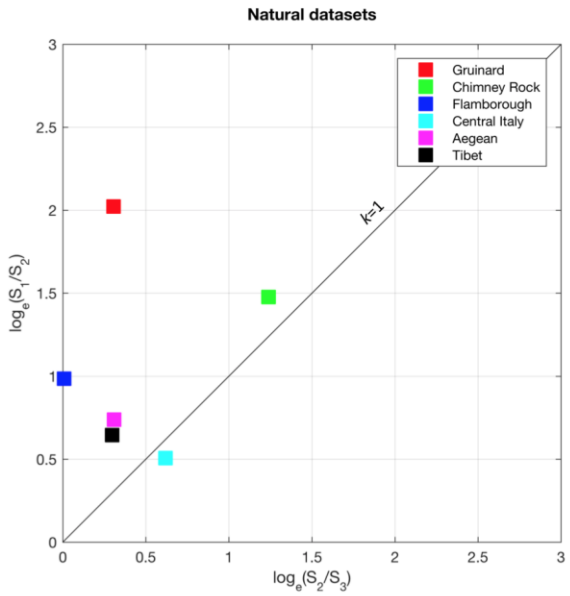

Figure 7. Eigenvalue ratio plot for the natural datasets shown in Figure 5. All but one dataset (Central Italy) lies above the line for k=1. The best-constrained quadrimodal fault dataset (Gruinard) has the highest ratio of $\log_e(S_1/S_2)$.

Field location		$S_1 - S_3$ test		$S_{11} - S_{33}$ test	
	n	p-value	# of modes	p-value	# of modes
Gruinard	75	0.00	> 2	0.00	> 2
Chimney Rock	86	0.99	2	1.00	2
Flamborough	346	0.00	> 2	0.00	> 2
Central Italy	1182	0.00	> 2	0.00	> 2
Aegean	156	0.00	> 2	0.00	> 2
Tibet	168	0.00	> 2	0.00	> 2

Table 3. p-values and corresponding decisions at 5% significance level of randomisation tests of bimodality for natural data sets. n=total sample size. B=999 further randomisation samples per data set (see text for details).

5. Discussion

In the analysis described above and the tests we performed with synthetic datasets, we assumed that bimodal and quadrimodal Watson orientation distributions provide a reasonable approximation to the distributions of poles to natural fault planes. In terms of the underlying statistics this is unproven, but we know of no compelling evidence in support of alternative distributions. New data from carefully controlled laboratory experiments on rock or analogous

materials might provide important constraints for the underlying statistics of shear fracture plane orientations.

We have tested our new methods on synthetic and natural datasets. Arguably, six natural datasets are insufficient to establish firmly the primacy of polymodal orthorhombic fault patterns in nature (Figure 7). However, we reiterate the key recommendation from Healy et al. (2015): to be useful for this task, fault orientation datasets need to show clear evidence of contemporaneity among all fault sets, through tools such as matrices of cross-cutting relationships (Potts & Reddy, 2000). In addition, as shown above, larger datasets (n>200) tend to show clearer patterns. Scope exists to collect fault or shear fracture orientation data from sources other than outcrops: Yielding (2016) has measured normal faults in seismic reflection data from the North Sea and Ghaffari et al. (2014) measured faults in cm-sized samples deformed in the laboratory and then scanned by X-ray computerised tomography.

The Chimney Rock dataset is probably not orthorhombic according to the two tests, and lies close to the line for k=1 on Figure 7. It is interesting to note that the Chimney Rock data, and other fault patterns from the San Rafael area of Utah, are considered as displaying orthorhombic symmetry by Krantz (1989) and Reches (1978). However, a subsequent re-interpretation by Davatzes et al. (2003) has ascribed the fault pattern to overprinting of earlier deformation bands by later sheared joints. This may account for the inconsistent results of our tests when compared to the position of the pattern on the eigenvalue plot. The Central Italy dataset (taken from Roberts, 2007) is very large (n=1182) and the data were measured over a wide geographical area. The dataset lies below the line for k=1 on the fabric eigenvalue plot (Figure 7), which might suggest it is bimodal. However, for fault planes measured over large areas there is a significant chance that regional stress variations may have produced systematically varying orientations of fault planes.

A final point concerns dispersion (noise) in the data. Synthetic datasets of bimodal (conjugate) and quadrimodal patterns with low values of κ, the Watson concentration parameter, fall into overlapping fields on the eigenvalue fabric plot. We ran 1000 Monte Carlo simulations of bimodal and quadrimodal Watson distributions each with n=52 poles, and κ = 5 and 10, and the results are shown in Figure 8. Bimodal (conjugate) datasets for these dispersed and sparse patterns lie across the 1:1 line on the fabric plot (Figure 8a; κ = 5 in blue, κ = 10 in yellow). Quadrimodal datasets for these parameters are also noisy, with some fabrics lying below the 1:1 line (Figure 8b; κ = 5 in blue, κ = 10 in yellow). Under these conditions of low κ (dispersed) and low n (sparse), it can be difficult to separate bimodal (conjugate) from quadrimodal fault patterns. However, we assert that this may not matter: a noisy and disperse 'bimodal' conjugate fault pattern is in effect similar to a polymodal pattern i.e. slip on these dispersed fault planes will produce a bulk 3D triaxial strain.

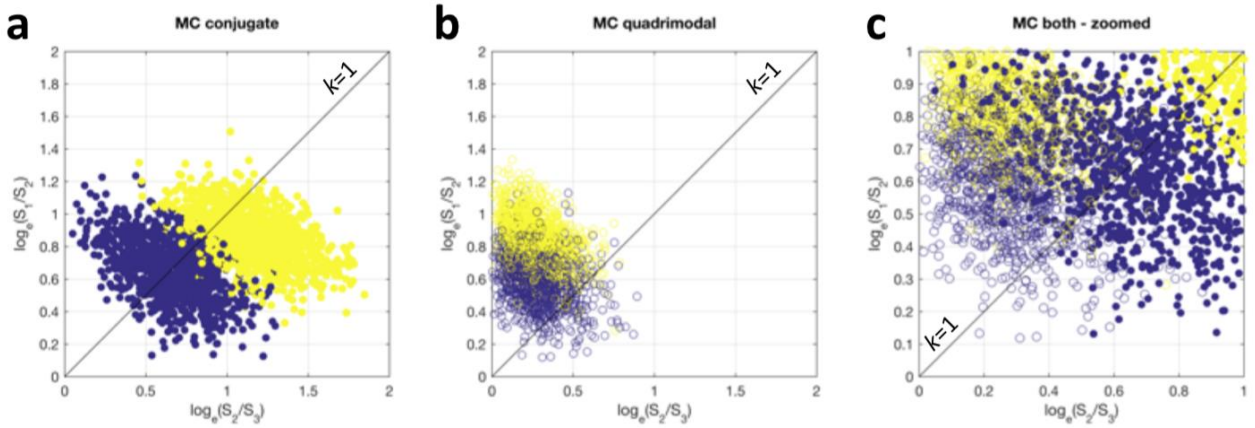

Figure 8. Eigenvalue ratio plots of synthetic data to illustrate the impact of dispersion on the ability of this plot to discriminate between conjugate (bimodal) and quadrimodal fault data. **a**) Monte Carlo ensemble of 2000 conjugate fault populations (mixtures of two equal Watson distributions), with κ varying from 5 (dark blue) to 10 (yellow). **b**) Monte Carlo ensemble of 2000 quadrimodal fault populations (mixtures of four equal Watson distributions), with κ varying from 5 (dark blue) to 10 (yellow). **c**) Data from a) and b) merged onto the same plot and enlarged to show the region close to the origin. Note the considerable overlap between the conjugate (bimodal) data with the quadrimodal data, especially for $\kappa = 5$ (dark blue).

To assess the relative performance of the two tests presented in this paper, we generated synthetic bimodal and quadrimodal distributions and compared the resulting p-values from applying both the S_1-S_3 and S_{11}-S_{33} tests to the same data. The results are shown in Figure 9, displayed as cross-plots of p(S_1-S_3) versus p(S_{11}-S_{33}). While there is a slight tendency for the p-values from the S_{11}-S_{33} test to exceed those of the S_1-S_3 test (i.e. the points tend on average to plot above the 1:1 line), neither of the tests can be said to 'better' or more 'accurate'. We therefore recommend the S_1-S_3 test as simpler and sufficient.

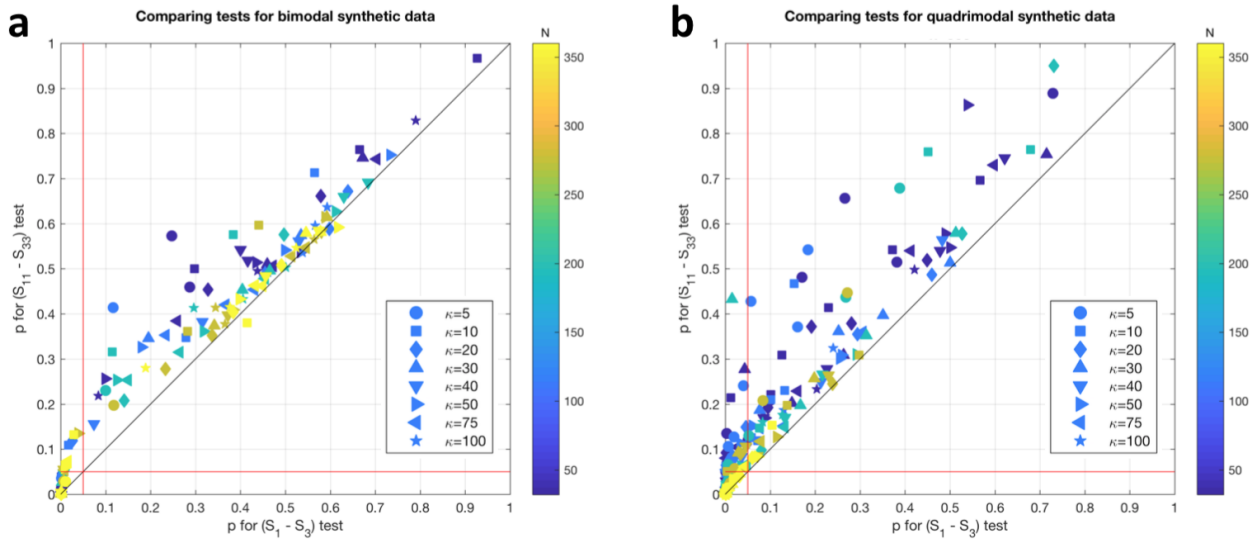

Figure 9. Eigenvalue ratio plots comparing the relative performance of the two tests proposed in this paper. The red lines denote p-values for either test at p=0.05, and the diagonal black line is the locus of points where p(S_1-S_3) = p(S_{11}-S_{33}). **a**) For bimodal synthetic datasets with size

(N) varying from 32-360 and concentration (κ) varying from 5-100, both tests perform well and reject the majority of the datasets ($p >> 0.05$). The p-values for the S_{11}-S_{33} test are, on average, slightly higher than those for the S_1-S_3 test across a range of dataset sizes and concentrations. **b**) For quadrimodal synthetic datasets, many of the p-values are < 0.05, and this especially true for the larger datasets (higher N, green/yellow). Smaller datasets (blue) can return p-values > 0.05.

6. Summary

Bimodal (conjugate) fault patterns form in response to a bulk plane strain with no extension in the direction parallel to the mutual intersection of the two fault sets. Quadrimodal and polymodal faults form in response to bulk triaxial strains and probably constitute the more general case for brittle deformation on a curved Earth (Healy et al., 2015). In this contribution, we show that distinguishing bimodal from quadrimodal fault patterns based on the orientation distribution of their poles can be achieved through the eigenvalues of the 2nd and 4th rank orientation tensors. We present new methods and new open source software written in R to test for these patterns. Tests on synthetic datasets where we controlled the underlying distribution to be either bimodal (i.e. conjugate) or quadrimodal (i.e. polymodal, orthorhombic) demonstrate that a combination of fabric eigenvalue (modified Flinn) plots and our new randomisation tests can succeed. Applying the methods to natural datasets from a variety of extensional normal-fault settings shows that 5 out of the 6 fault patterns considered here are probably polymodal. The most tightly constrained natural dataset (Gruinard) displays clear orthorhombic symmetry and is unequivocally polymodal. We encourage other workers to apply these tests to their own data and assess the underlying symmetry in the brittle fault pattern and to consider what this means for the causative deformation.

Acknowledgements

DH gratefully acknowledges receipt of NERC grant NE/N003063/1, and thanks the School of Geosciences at the University of Aberdeen for accommodating a period of research study leave, during which time this paper was written.

References

Aydin, A., & Reches, Z. E. 1982. Number and orientation of fault sets in the field and in experiments. *Geology*, *10*(2), 107-112.

Blenkinsop, T. G. 2008. Relationships between faults, extension fractures and veins, and stress. *Journal of Structural Geology*, *30*(5), 622-632.

Davatzes, N.C., Aydin, A. and Eichhubl, P., 2003. Overprinting faulting mechanisms during the development of multiple fault sets in sandstone, Chimney Rock fault array, Utah, USA. *Tectonophysics*, *363*(1-2), pp.1-18.

401 Ekström, G., Nettles, M., & Dziewoński, A. M. 2012. The global CMT project 2004–2010:
402 Centroid-moment tensors for 13,017 earthquakes. *Physics of the Earth and Planetary Interiors*,
403 *200*, 1-9.

404 Fisher, N.I., Lewis, T. and Embleton, B.J., 1987. *Statistical analysis of spherical data*. Cambridge
405 University Press.

406 Flinn, D. 1962. On folding during three-dimensional progressive deformation. *Quarterly Journal*
407 *of the Geological Society*, *118*(1-4), 385-428.

408 Ghaffari, H. O., Nasseri, M. H. B., & Young, R. P. 2014. Faulting of Rocks in a Three-Dimensional
409 Stress Field by Micro-Anticracks. *Scientific reports*, *4*, 5011.

410 Healy, D., Jones, R.R. and Holdsworth, R.E., 2006a. Three-dimensional brittle shear fracturing
411 by tensile crack interaction. *Nature*, *439*(7072), pp.64-67.

412 Healy, D., Jones, R.R. and Holdsworth, R.E., 2006b. New insights into the development of brittle
413 shear fractures from a 3-D numerical model of microcrack interaction. *Earth and Planetary*
414 *Science Letters*, *249*(1), pp.14-28.

415 Healy, D., Blenkinsop, T.G., Timms, N.E., Meredith, P.G., Mitchell, T.M. and Cooke, M.L., 2015.
416 Polymodal faulting: Time for a new angle on shear failure. *Journal of Structural Geology*, *80*,
417 pp.57-71.

418 Krantz, R. W. 1989. Orthorhombic fault patterns: the odd axis model and slip vector
419 orientations. *Tectonics*, *8*(3), 483-495.

420 Lisle, R. J., & Leyshon, P. R. 2004. *Stereographic projection techniques for geologists and civil*
421 *engineers*. Cambridge University Press.

422 Mardia, K.V. & Jupp, P.E., 2000. *Directional statistics*. John Wiley & Sons.

423 McCormack, K.D. & McClay, K.R., 2018. Orthorhombic faulting in the Beagle Sub-basin, North
424 West Shelf, Australia. *Geological Society, London, Special Publications*, *476*.

425 Peacock, D. C. P., & Sanderson, D. J. 1992. Effects of layering and anisotropy on fault geometry.
426 *Journal of the Geological Society*, *149*(5), 793-802.

427 Potts, G. J., & Reddy, S. M. 2000. Application of younging tables to the construction of relative
428 deformation histories—1: fracture systems. *Journal of Structural Geology*, *22*(10), 1473-1490.

429 R Core Team, 2017. *R: A language and environment for statistical computing*. R Foundation for
430 Statistical Computing, Vienna, Austria. URL https://www.R-project.org/.

431 Ramsay, J. 1967. Folding and fracturing of rocks.

432 Reches, Z. E. 1978. Analysis of faulting in three-dimensional strain field. *Tectonophysics*, *47*(1-
433 2), 109-129.

434 Reches, Z. E. 1983. Faulting of rocks in three-dimensional strain fields II. Theoretical analysis.
435 *Tectonophysics*, *95*(1-2), 133-156.

436 Reches, Z. E., & Dieterich, J. H. 1983. Faulting of rocks in three-dimensional strain fields I. Failure
437 of rocks in polyaxial, servo-control experiments. *Tectonophysics*, *95*(1-2), 111-132.

438 Roberts, G. P. 2007. Fault orientation variations along the strike of active normal fault systems
439 in Italy and Greece: Implications for predicting the orientations of subseismic-resolution faults
440 in hydrocarbon reservoirs. *AAPG bulletin*, *91*(1), 1-20.

441 Scheidegger, A. E. 1965. On the statistics of the orientation of bedding planes, grain axes, and
442 similar sedimentological data. *US Geological Survey Professional Paper*, *525*, 164-167.

443 Woodcock, N.H., 1977. Specification of fabric shapes using an eigenvalue method. *Geological*
444 *Society of America Bulletin*, *88*(9), pp.1231-1236.

445 Yielding, G., 2016. The geometry of branch lines. In: Childs, C., Holdsworth, R. E., Jackson, C. A.-
446 L., Manzocchi, T., Walsh, J. J. & Yielding, G. (eds). *The Geometry and Growth of Normal Faults*.
447 Geological Society, London, Special Publications, 439.

448